International Journal of Microwave and Wireless Technologies

cambridge.org/mrf

Exploring the possibility to minimize the clutter for contrast target detection with MIMO-based through-wall imaging system

Suman Anand[1], Shailza Gotra[2], Vineet Singh[3], Mandar Bivalkar[4] and Dharmendra Singh[1]

[1]Department of Electronics and Communication Engineering, Indian Institute of Technology Roorkee, Roorkee, India; [2]Department of Electronics and Communication Engineering, The LNM Institute of Information Technology (LNMIIT), Jaipur, India; [3]Department of Electronics and Communication Engineering, National Institute of Technology Patna, Patna, India and [4]Department of Computer Engineering, K. J. Somaiya Institute of Technology, Mumbai, India

Research Paper

Cite this article: Anand S, Gotra S, Singh V, Bivalkar M, Singh D (2026) Exploring the possibility to minimize the clutter for contrast target detection with MIMO-based through-wall imaging system. *International Journal of Microwave and Wireless Technologies* **18**(4), 647–660. https://doi.org/10.1017/S1759078726103468

Received: 10 September 2025 UTC
Revised: 28 May 2026 UTC
Accepted: 29 May 2026 UTC
First published online: 20 July 2026 UTC

Keywords:
clutter reduction; contrast dielectric targets detection; multiple-input multiple-output (MIMO); through-wall imaging (TWI)

Corresponding author: Dharmendra Singh; Email: dharmfec@gmail.com

Abstract

In recent years, the through-wall imaging (TWI) systems have garnered tremendous interest due to their potential applications in surveillance, search–rescue operations, and security monitoring, enabling the detection and visualization of objects behind opaque obstacles such as walls. The multiple-input multiple-output (MIMO) TWI system has been developed to detect hidden targets behind walls. MIMO-based TWI considerably reduces the time it takes to scan the walls. This study presents an experimental evaluation of a MIMO-based TWI system using a dataset of targets with varying dielectric properties placed at uniform and nonuniform distances behind a wall. The B-scan data are collected for different types of targets for contrast target detection. To effectively suppress clutter and enhance target detectability, we employed a range of advanced signal processing techniques, including singular value decomposition (SVD), SVD-based noise subspace exploitation, the optimum shrinkage algorithm, and background subtraction using data-driven thresholding. The target-to-clutter ratio of the final image was computed to evaluate the effectiveness of each clutter removal technique and to facilitate a comparative analysis of the results. The imaging results demonstrated that the system could detect single and multiple targets, including those composed of different materials.

Introduction

Through-wall imaging (TWI) using radar systems has gained prominence and significant attention in recent years due to its potential applications in military surveillance, search–rescue operations, and security systems [1, 2]. These systems enable the detection and localization of obscured objects or individuals behind visually opaque structures, such as walls made of dielectric materials [3, 4]. Using microwave-frequency electromagnetic radiation, TWI may detect objects concealed behind walls. Recent works [5, 6] have investigated the potential use of multiple-input multiple-output (MIMO) setups. However, TWI poses several challenges due to signal attenuation, wall-induced clutter, multipath propagation, and variability in wall and target properties. MIMO-based through-wall radar imaging has emerged as a promising solution among the various radar technologies. Using spatial diversity and virtual aperture expansion in the MIMO system led to reduced scan and acquisition times, improved image resolution, and an enhanced signal-to-noise ratio. In the TWI system, complexities arise due to variations in signal reception at virtual nodes, clutter suppression difficulties, and deviations from ideal propagation models, which affect image formation and accurate target estimation. This study fills such gaps by looking at how to optimize and build TWI systems that use MIMO. The reliability and accuracy of through-wall target identification and imaging are examined in the research by examining the effects of several MIMO array designs, clutter mitigation approaches, and signal processing algorithms.

Various research studies have investigated hardware architectures for microwave imaging systems, including synthetic aperture radar (SAR), phased array radar, and MIMO radar systems. Phased array-based systems offer high precision and rapid data acquisition but come with the drawback of complex hardware designs [7, 8, 9]. In contrast, SAR systems require less hardware but operate at a slower pace due to extended data acquisition times. The advantage of MIMO-based systems is that they provide an optimal balance between reduced acquisition time and hardware complexity. The integration of MIMO antennas has significantly enhanced radar performance by improving angular resolution, aspect angle coverage, system gain, and beam steering [10].

© The Author(s), 2026. Published by Cambridge University Press in association with The European Microwave Association.

Table 1. System parameters for the MIMO TWI system

Parameters	Specifications
Radar type	SFCW
MIMO element	4 × 4 Tx/Rx
Operational frequency	1.5–3.5 GHz
Antenna type	Vivaldi
Antenna element gain	6–7 dBi
Transceiver dynamic range	100 dB
Transmitted power	+5 dBm
Wall distance from the MIMO systems	50 cm

Despite these advancements, the application of MIMO technology in TWI remains relatively underexplored, resulting in a limited body of literature. Frequency-diversified arrays, as discussed in [11, 12], require careful optimization in terms of frequency increments and statistical methods. Notably, a study conducted on comparing singular value decomposition (SVD), principal component analysis (PCA), independent component analysis (ICA), and factor analysis determined that ICA achieved optimal performance in detecting low dielectric materials located behind walls. In this work, we propose a wideband MIMO-inspired imaging system that addresses the limitations of existing approaches by employing a time-division multiplexing strategy. The proposed system features a 4 × 4 planar MIMO array and its system parameters are listed in Table 1. Its performance is evaluated through simulations, experimental validation, and signal processing techniques applied to the collected data. When utilizing the MIMO array for faster data acquisition, the channel formed by its virtual nodes influences the aspect angle from which the scenario is observed. This results in variations in the received signal at the virtual nodes compared to the signal strength recorded at the same positions while using a single scanning antenna. These deviations in signal strength impede the generation of B-scan images, ultimately affecting the accurate estimation of target size in the C-scan representation of the scene.

This paper is structured with the second section, which outlines the experimental setup and signal model employed for TWI. The third section outlines the methodology for image reconstruction; the fourth section discusses various techniques for clutter reduction to enhance image contrast, along with the results and their analysis; and the fifth section summarizes the paper's findings.

Experimental setup and signal model

The system comprises a 4 × 4 MIMO planar array, Radio Frequency (RF) transceiver, a system processor, a MIMO antenna selector, a display, and memory. The MIMO antenna array consists of four horizontal rows, each containing four vertically arranged antennas, forming a 4 × 4 planar configuration. The system operates in the 1.5–3.5 GHz frequency range, selected to achieve a balance between penetration depth and resolution for TWI. The attenuation of electromagnetic waves in lossy media (e.g., brick or concrete) increases with frequency and can be expressed as $\alpha \infty f\sqrt{u \in}$ also at higher frequencies (above ~6 GHz); attenuation becomes significant, resulting in poor penetration through the wall. Although the proposed methodology can be extended to mmWave frequencies, severe attenuation limits its applicability for TWI. The designed imaging system consists of three main parts: transceiver, control unit, and MIMO array. The RF signal is generated inside the transceiver and goes to the MIMO antenna array; however, the control unit is responsible for the time synchronization between the correct elements selection and triggering the frequency sweeps of the transceiver. This arrangement enables efficient data acquisition for TWI applications.

The schematic diagram of the MIMO TWI system is shown in Figure 1. A graphical user interface (GUI) is integrated into the system to facilitate data analysis and visualization. The GUI provides options for applying post-processing algorithms and enables real-time display of imaging results. The system is designed with a MIMO configuration, incorporating a 4 × 4 array of transmitters and receivers (Tx/Rx). This arrangement enhances signal processing capabilities, allowing for improved imaging and target detection operating within a frequency range of 1.5–3.5 GHz; the system ensures effective penetration and resolution for TWI applications. This frequency band is suitable for detecting and identifying objects behind obstacles while maintaining a balance between penetration depth and image clarity. A Vivaldi antenna is employed due to its broadband characteristics and high directivity, making it an ideal choice for microwave imaging applications. The antenna elements provide a gain ranging from 6 to 7 dBi in the passband, contributing to efficient signal transmission and reception. The transceiver dynamic range of 100 dB ensures a high sensitivity to weak signals, allowing for better differentiation between targets and background noise. Additionally, the system operates with a transmitted power of +5 dBm, ensuring optimal performance while minimizing interference. The system is positioned at 50 cm from the wall for effective imaging. This setup allows for accurate data acquisition and processing, enabling reliable detection and identification of objects behind the wall.

Methods and methodology

Data collection

In TWI systems, data acquisition commonly utilizes three scanning modalities: A-scan, B-scan, and C-scan. Our experimental setup generates B-scan data by stacking sequential A-scans acquired at uniformly spaced positions along the cross-range axis. The step size between these acquisition points is determined by the antenna's aperture, which defines the cross-range resolution of the system.

Each A-scan represents the received radar signal (echo) as a function of time (or range) at a specific antenna position.

Figures 2–5 show raw B-scan images obtained when targets were placed behind the wall at varying distances. This figure sets the raw data quality before applying any clutter removal methods, justifying the need for further signal processing.

As the MIMO-based TWI system translates linearly across the scene, a 2D B-scan image is constructed by concatenating these A-scans. The resulting B-scan represents the cross-range vs down-range profile of the scene, effectively mapping the location and relative dielectric contrast of objects behind the wall. In our experiments, various dielectric materials, including metal, wood, and Teflon, are placed behind the wall at either distinct or identical distances. The variations in dielectric properties and placement enable the assessment of the system's capability to detect, distinguish, and localize different materials through the wall. This

https://doi.org/10.1017/S1759078726103468 Published online by Cambridge University Press

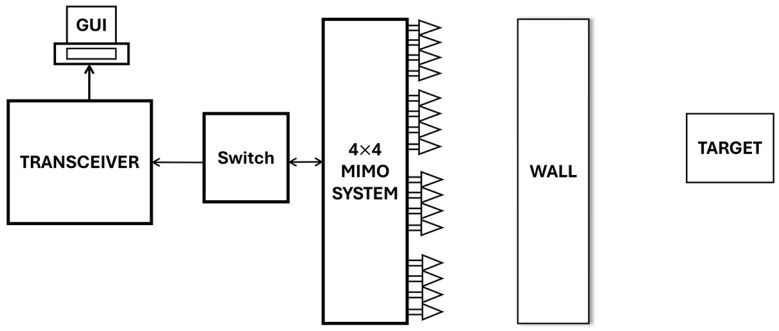


Figure 1. Schematic diagram for MIMO TWI system.

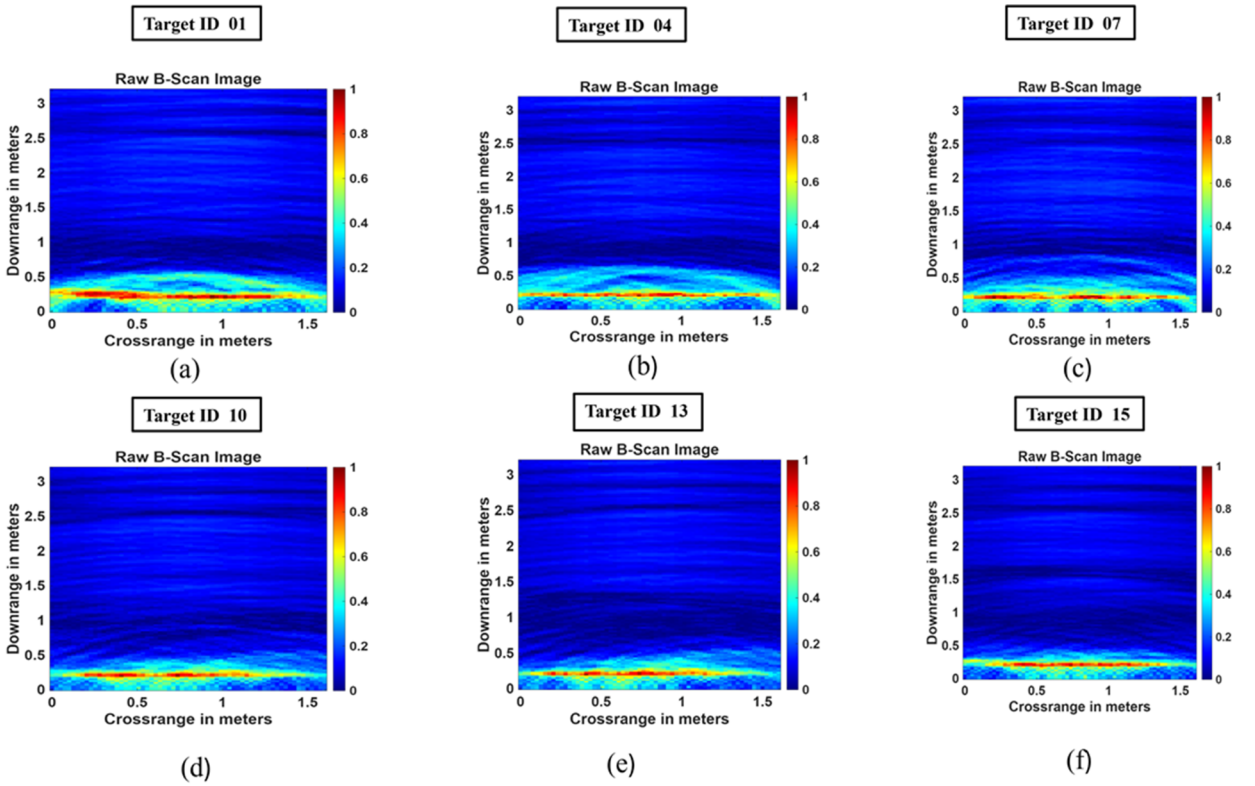


Figure 2. Raw B-scan images for different datasets consisting of metallic targets (Ref. Table 3. Target IDs: 01, 04, 07, 10, 13, and 15).

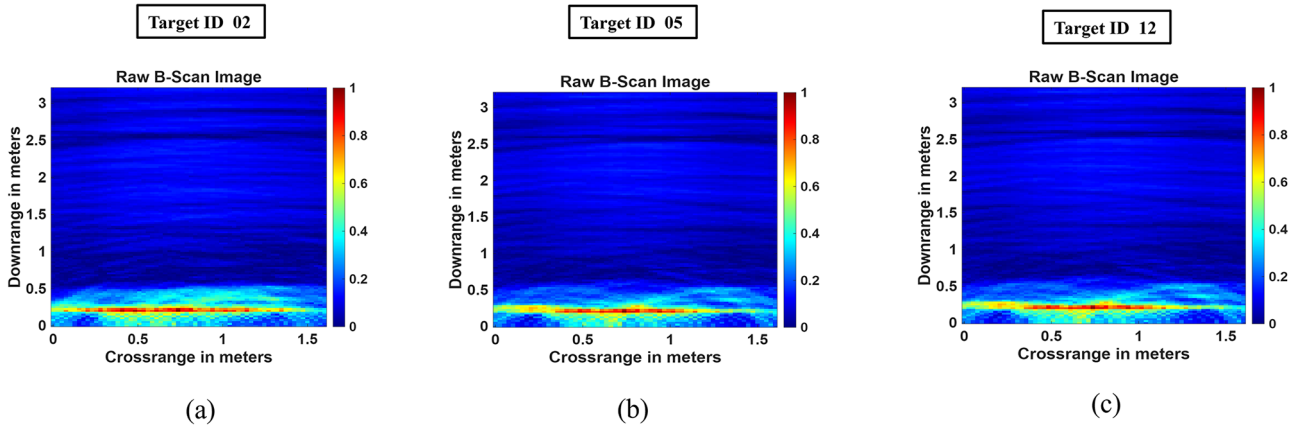


Figure 3. Raw B-scan images for different datasets consisting of wood targets (Ref. Table 3. Target IDs: 02, 05, and 12).

https://doi.org/10.1017/S1759078726103468 Published online by Cambridge University Press

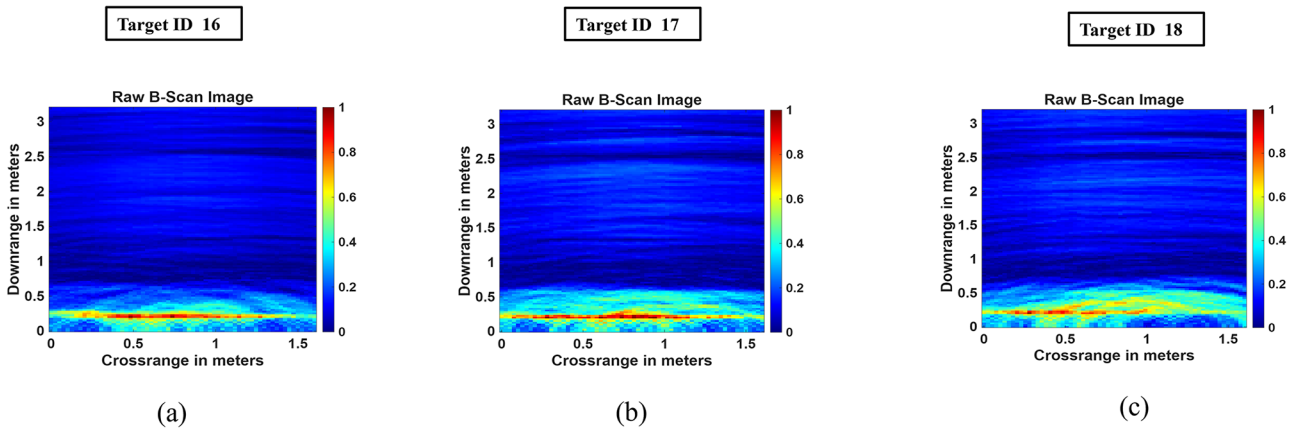


Figure 4. Raw B-scan images for different datasets consisting of two different target combinations (Ref. Table 3. Target IDs: 16, 17, and 18).

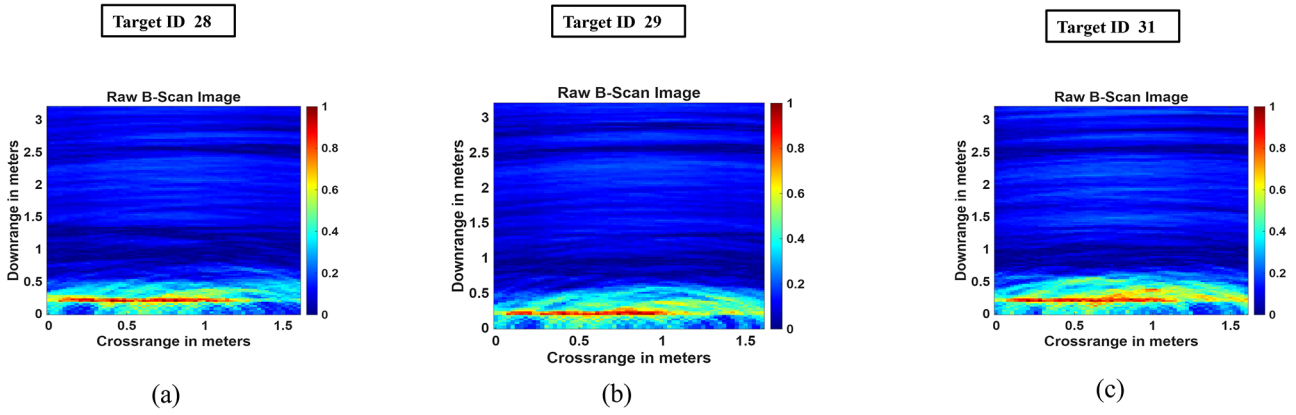


Figure 5. Raw B-scan images for different datasets consisting of three target combinations (Ref. Table 3. Target IDs: 28, 29, and 31).

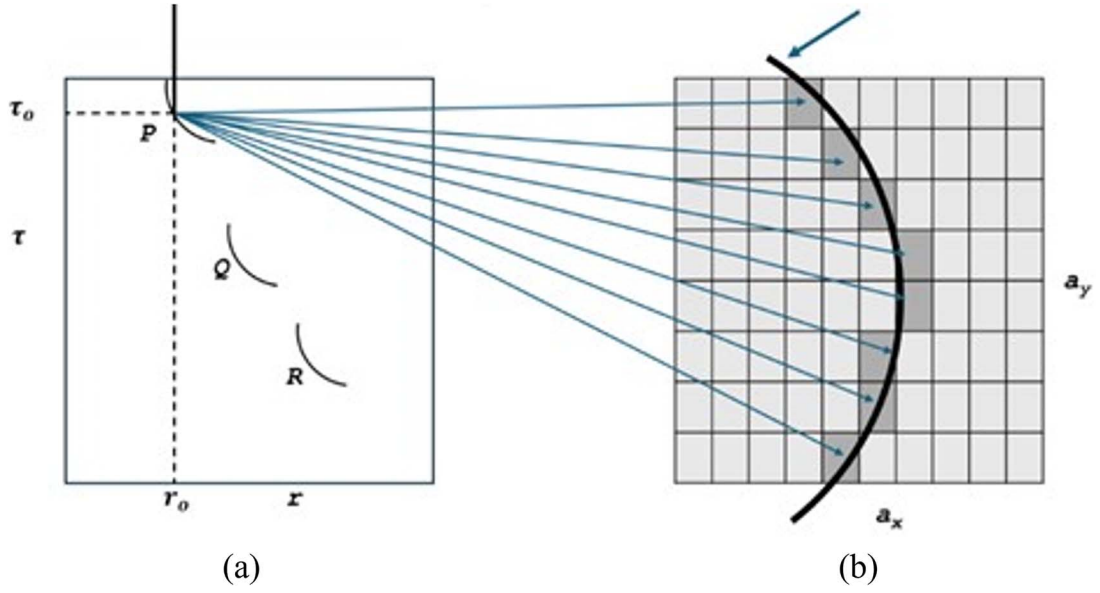


Figure 6. (a) Echo data after fast time compression $S(t_0, \tau_0)$. (b) Grid of imaging areas with the same time delay.

linear scanning approach, in combination with MIMO radar architecture, enhances spatial resolution and target detection performance, making it suitable for reliable through-wall surveillance applications.

Reconstruction of images using the back projection algorithm

The image reconstruction algorithms are the fundamental component of a microwave imaging system. In this work, we have used the back projection algorithm to reconstruct the image behind the

https://doi.org/10.1017/S1759078726103468 Published online by Cambridge University Press

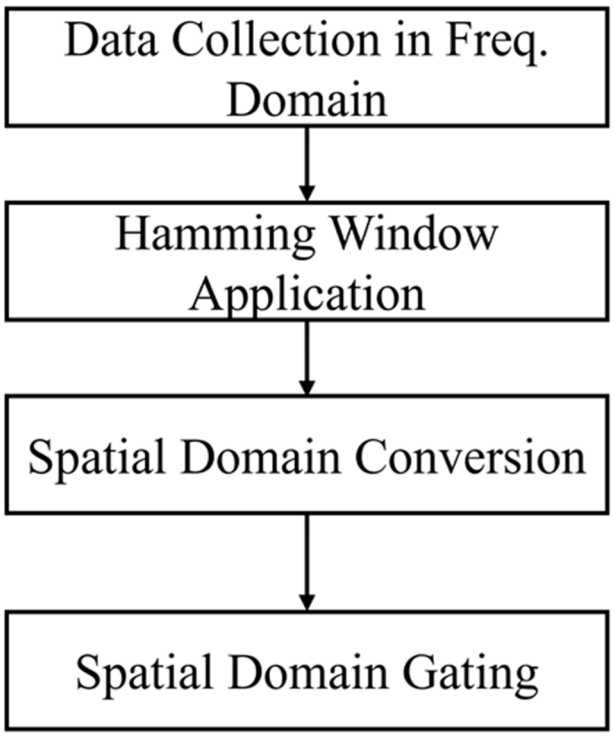


Figure 7. Pre-processing steps of the collected data.

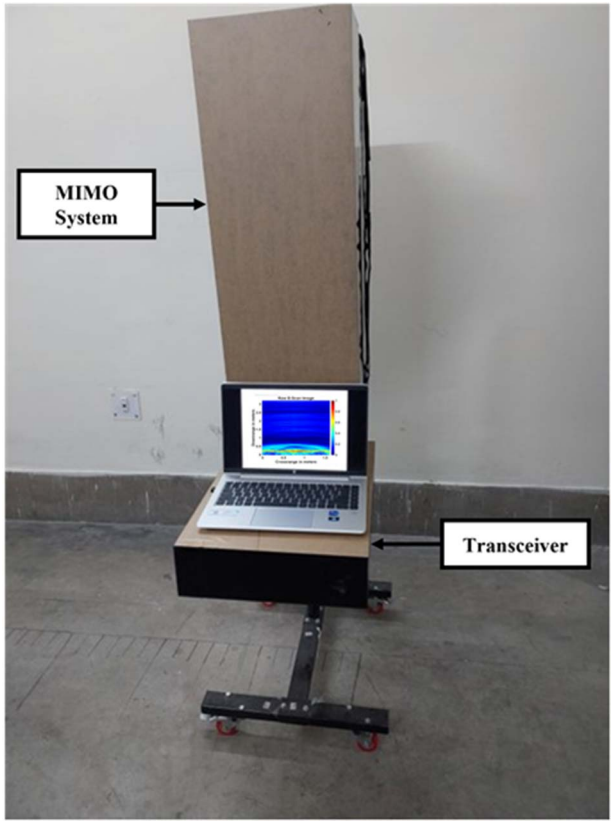


Figure 8. Developed a MIMO-based TWI system.

wall scenario. Figure 6 illustrates the image reconstruction methods for TWI scenario. The data for each received signal represents a set of signal intensity values as a function of time delay. The signal received in a given bin at the given instant is from all pixel locations where the total flight time equals this specific time bin. The back projection technique consists of recording the amplitude of each time bin on a spatial time grid. Each channel's recorded amplitudes are then added together on the spatial grid. Mathematically, in free space, the back-projected signal at pixel (x_i,y_i) in the scanning area image plane is given by

$$I(x_i, y_i) = \sum_n E[t_i(n), n] \tag{1}$$

where

$$t_i = (R_{Txi} + R_{Rxi}(n))/c \tag{2}$$

$$R_{Txi} = \sqrt{(x_i - x_T)^2 + (y_i - y_T)^2} \tag{3}$$

$$R_{Rxi}(n) = \sqrt{(x_i - x_R(n))^2 + (y_i - y_R(n))^2} \tag{4}$$

where each symbol has the usual meaning as

c: speed of light
I: pixel amplitude
t: time
x and y: pixel coordinate in m
n: receiver number.

The pre-processing steps for the collected data are given in Figure 7.

The developed MIMO-based TWI system is shown in Figure 8. The collected data is passed through a Hamming window, which results in an improved spectral response in the stored data. The step involves the conversion of frequency domain data into time domain data, which can be obtained using the following equation.

$$D(z) = \sum_{n=0}^{N-1} D(f)\, e^{(j2\pi f_n(2z/c))} \tag{5}$$

where $D(f)$ is the raw data in the frequency domain, f_n is the operating frequency, N is the number of frequency points, z is the downrange distance in cm, and $D(z)$ is the data in the spatial domain. This spatial domain conversion gives the range profile corresponding to a single A-scan data captured from a single point of the scanning plane. Now, the RF section of the design, through which the high-frequency signal passes, encounters impedance mismatches in the different circuit components, leading to reflections at multiple distances in the range profile. Once the RF circuit is fixed, these reflections are constant and can be omitted using spatial domain gating. Once the data is spatially gated, it is ready for the imaging algorithm application.

Post-processing techniques

TWI using radar systems captures raw data that is often degraded due to wall-induced distortions, multipath propagation, and environmental noise. To address these challenges, post-processing techniques play a vital role in suppressing wall clutter, enhancing the signal-to-clutter ratio, accurately localizing targets, and improving overall image resolution. In recent years, subspace-based methods have emerged as prominent clutter removal

https://doi.org/10.1017/S1759078726103468 Published online by Cambridge University Press

Table 2. Time and space complexity for different algorithms

Algorithm	Dominant operation	Time complexity	Space complexity
SVD	Full matrix decomposition	$(O(N^3))$	$(O(N^2))$
SVD noise subspace	SVD + projection	$(O(N^3))$	$(O(N^2))$
Optimal shrinkage	SVD + shrinkage	$(O(N^3))$	$(O(N^2))$
Background subtraction	Mean and threshold ops	$(O(N^2))$	$(O(N^2))$

Note: Where $O(N^n)$ represents a proportional increase in complexity with the input size of the matrix N.

approaches. Techniques such as SVD, PCA, ICA, and background subtraction have been widely adopted to effectively isolate and eliminate wall reflections and background interference from the radar data.

Singular value decomposition (SVD)

This powerful linear algebra technique analyses and reconstructs images, reduces noise, compresses data, or extracts essential features. It is the most efficient technique from linear algebra for clutter reduction. SVD of the B-scan matrix (S) of dimension $M \times N$ is given by:

$$S = UDV^T \tag{6}$$

where $U = [U_1, U_2, \ldots, U_M]$ and $V = [V_1, V_2, \ldots, V_N]$ are the left and right singular matrices whose columns are eigenvectors. The D matrix is the diagonal matrix for which singular values are arranged in decreasing order. Basically, U and V are the eigenvectors of $\{SS^T\}$ and $\{S^TS\}$.

SVD noise-space exploitation

SVD noise-space exploitation techniques are widely employed in TWI and array signal processing to distinguish the target (signal) subspace from the clutter or noise subspace. These methods leverage the mathematical properties of SVD to separate signal and noise components based on singular value or eigenvalue thresholding. Unlike conventional SVD-based filtering, which typically reconstructs the signal using dominant singular components, noise-space exploitation selectively reconstructs the image using higher-order singular components. This approach suppresses strong background signals, such as wall echoes, and enhances weaker signal returns that may correspond to concealed targets. By focusing on the so-called "noise subspace," this technique enables improved detection of low-reflectivity or deeply embedded targets that might be obscured in traditional processing frameworks.

Data-driven thresholding background subtraction methods

Data-driven thresholding background subtraction effectively suppresses strong static components, such as wall echoes, in radar-based TWI. This technique enhances the visibility of dynamic or concealed targets by adaptively identifying and removing background clutter. Unlike fixed-threshold methods, it employs a dynamic threshold derived from image statistics such as mean, standard deviation, or percentile values to differentiate between background and potential target reflections. The method enables improved target isolation by zeroing out components below the threshold and preserving only significant deviations, particularly in complex and cluttered environments.

OptShrink algorithms

OptShrink is a sophisticated method for cleaning up noisy matrix data, mainly when the data is known to have a low-rank structure [13, 14]. It has applications in various fields, including signal processing, image processing, and functional MRI reconstruction. OptShrink algorithm re-weights the singular value of the measurement matrix buried in the noise optimally. The principle used in [13] is from random matrix theory, consider a signal plus noise or clutter matrix $\tilde{X} = S_n + X_n$, where $\tilde{X}$ is the received signal, S_n is the transmitted signal, and X_n is the random noise or clutter. After implementing SVD $S_n = \sum_{I=1}^{r} \theta_i u_i v_i^H$, where u_i and v_i are the left and right unitary matrices; θ_i are the singular values of the matrix S_n. In the Eckart–Young–Mirsky (EYM) estimator, the objective is to find an estimate of the low-rank signal matrix if the rank r is known. The solution for the optimization problem for Frobenius norm $\|.\|_F$ is the constrained optimization problem such that $= \underset{rank(S)=r}{\arg\, min} X\, S_{nF}$, and $S_{eym} = \sum_{I=1}^{r} \sigma_i u_i v_i^H$ is the SVD of the $\tilde{X}$, and it is also maximum likelihood estimation. If X_n is assumed to be independent and identically distributed (IID) Gaussian, a natural extension for this is available when S_n is the low rank and has some exploitable structure, such as low rank and sparse [15]. This estimation in EYM can be improved when an exploitable structure other than a low rank is considered. Let us consider that S_n and X_n are independent, and X_n is a random matrix that is bi-orthogonally invariant, i.e., its distribution is invariant when the right (or left) singular vectors are multiplied. If S_n is isotopically random, then X_n need not be random. Hence, the OptShrink algorithm is applicable to Gaussian and non-Gaussian cases. D-transform, i.e., the analog form of the Fourier transform, is used to find the optimum rank r in the following manner. The effective rank for the SVD matrix is estimated

1) Compute SVD for R by $\hat{R} = \sum_{q}^{i=1} \hat{\sigma}_i u_i v_i^T$
2) Compute $\hat{\Sigma} = \text{diag}(\sigma_{\hat{r}+1}, \ldots, \sigma_q) \in \mathbb{R}^{(n-\hat{r})\times(m-\hat{r})}$.
3) Compute D-transform for $\hat{D}\left(\hat{\sigma}_i, \hat{\Sigma}_{\hat{r}}\right)$ and $\hat{D}'(\hat{\sigma_i}, \sum_{\hat{r}})$

$$\hat{D}(z,x) = 1/nTr\left(z\left(z^2I - xx^H\right)\right) \cdot 1/mTr\left(z\left(z^2I - x^Hx\right)^{-1}\right)$$

Table 2 compares computational complexity estimated for different clutter reduction methods described above

Results and discussion

Table 3 presents a structured dataset compiled from an extensive experimental study conducted to assess the performance of a MIMO-based TWI system under diverse operational conditions. The experiments involve targets composed of three representative materials – metal, wood, and Teflon chosen for their distinct dielectric properties. This selection enables evaluation of the system's sensitivity to varying electromagnetic characteristics. The study systematically progresses from single-target to two- and three-target configurations, thereby facilitating performance assessment

https://doi.org/10.1017/S1759078726103468 Published online by Cambridge University Press

Table 3. Description of the targets

Target ID	No of targets	Target type	Distance(s) of the targets from the wall (cm)	Target description
01	01	Metal	20	30 cm × 30 cm
02	01	Wood	20	50 cm × 50 cm
03	01	Teflon	20	Circular Teflon of radius 15 cm
04	01	Metal	50	30 cm × 30 cm
05	01	Wood	50	50 cm × 50 cm
06	01	Teflon	50	Circular Teflon of radius 15 cm
07	01	Metal	85	30 cm × 30 cm
08	01	Wood	85	50 cm × 50 cm
09	01	Teflon	85	Circular Teflon of radius 15 cm
10	01	Metal	100	30 cm × 30 cm
11	01	Teflon	100	Circular Teflon of radius 15 cm
12	01	Wood	100	50 cm × 50 cm
13	01	Metal	150	30 cm × 30 cm
14	01	Metal	200	30 cm × 30 cm
15	01	Wood	150	50 cm × 50 cm
16	02	Metal–wood	50 and 50	30 cm × 30 cm and 50 cm × 50 cm
17	02	Metal–Teflon	50 and 50	30 cm × 30 cm and circular Teflon of radius 15 cm
18	02	Wood–Teflon	50 cm and 50 cm	50 cm × 50 cm and circular Teflon of radius 15 cm
19	02	Metal–wood	100 cm and 100 cm	30 cm × 30 cm and 50 cm × 50 cm
20	02	Metal–Teflon	75 cm and 75 cm	30 cm × 30 cm and circular Teflon of radius 15 cm
21	02	Wood–Teflon	50 cm and 75 cm	50 cm × 50 cm and circular Teflon of radius 15 cm
22	02	Metal–wood	75 cm and 50 cm	30 cm × 30 cm and 50 cm × 50 cm
23	02	Metal–Teflon	100 cm and 50 cm	30 cm × 30 cm and circular Teflon of radius 15 cm
24	02	Wood–Teflon	100 cm and 50 cm	50 cm × 50 cm and circular Teflon of radius 15 cm
25	02	Metal–wood	30 cm and 50 cm	30 cm × 30 cm and 50 cm × 50 cm
26	02	Metal–Teflon	75 cm and 50 cm	30 cm × 30 cm and circular Teflon of radius 15 cm
27	02	Wood–Teflon	30 cm and 50 cm	50 cm × 50 cm and circular Teflon of radius 15 cm
28	03	Metal–wood–Teflon	100–50–30	30 cm × 30 cm, 50 cm × 50 cm, and circular Teflon of radius 15 cm
29	03	Metal–wood–Teflon	150–100–30	30 cm × 30 cm, 50 cm × 50 cm, and circular Teflon of radius 15 cm
30	03	Metal–wood–Teflon	150–75–85	30 cm × 30 cm, 50 cm × 50 cm, and circular Teflon of radius 15 cm
31	03	Metal–wood–Teflon	50–50–50	30 cm × 30 cm, 50 cm × 50cm, and circular Teflon of radius 15 cm



Figure 9. Contrast targets placed behind the wall.

https://doi.org/10.1017/S1759078726103468 Published online by Cambridge University Press

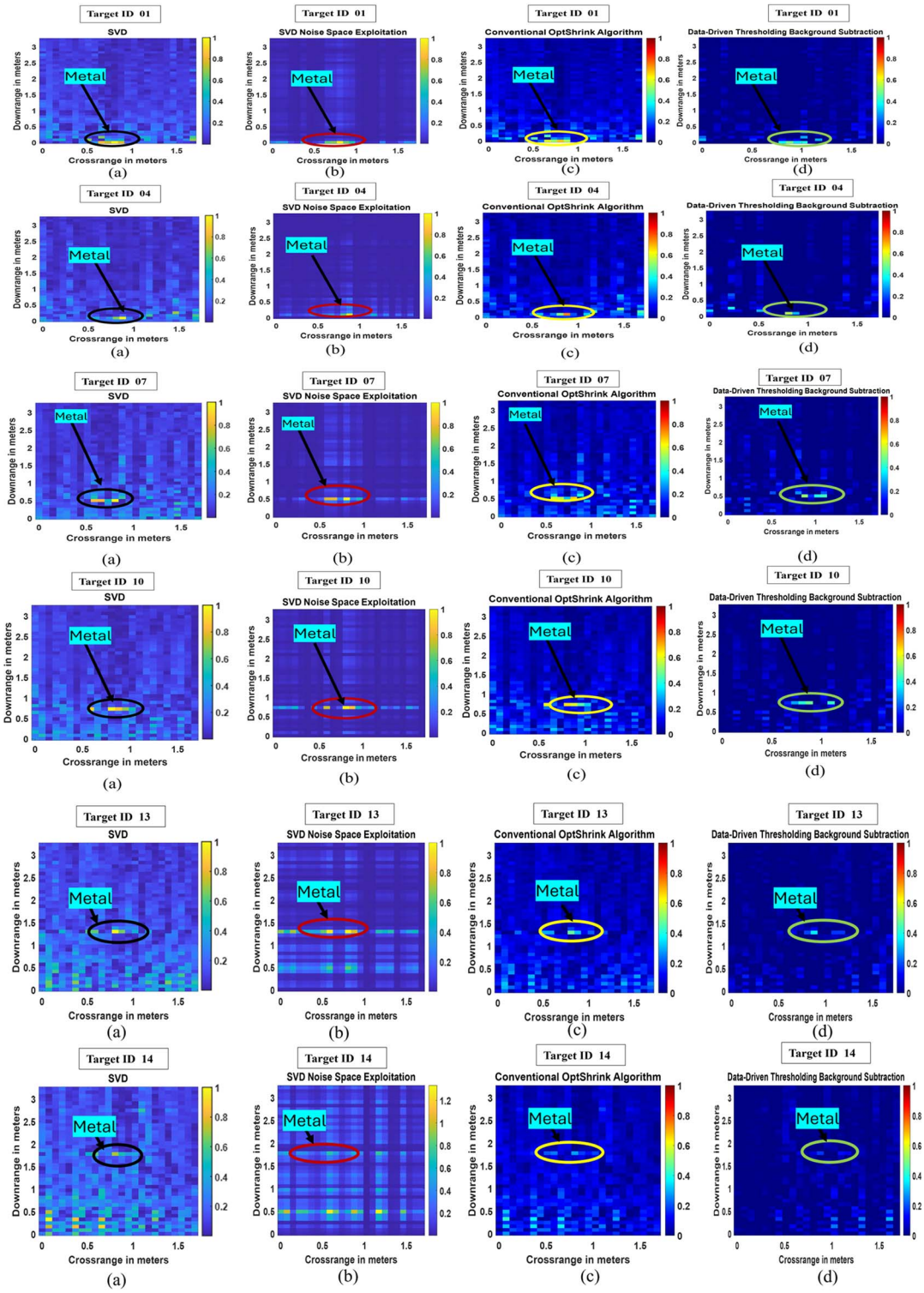


Figure 10. Reconstructed images for metal targets with (a) SVD, (b) SVD noise exploitation, (c) conventional OptShrink algorithm, and (d) thresholding background subtraction.

under increasingly complex detection scenarios. The target distance is varied from 20 to 200 cm, allowing investigation into the effects of propagation loss, signal attenuation, and spatial resolution. Target dimensions are also varied, comprising square and circular geometries of different sizes (as detailed in Table 3), to analyze the system's responsiveness to size-dependent scattering behavior. Each experimental scenario is conducted within an enclosed indoor environment, with the imaging system positioned in an adjacent room to emulate realistic through-wall conditions. Each experimental scenario is conducted within an enclosed indoor

https://doi.org/10.1017/S1759078726103468 Published online by Cambridge University Press

Table 4. Performance of clutter reduction algorithms based on TCR for a single metallic target

Techniques	TCR (dB)					
	Target ID 01	Target ID 04	Target ID 07	Target ID 10	Target ID 13	Target ID 14
SVD	17.19	11.98	9.24	7.56	5.23	3.26
SVD noise exploitation	7.97	14.13	5.40	1.26	5.258	2.56
Convention OptShrink algorithm	8.20	8.43	7.57	2.56	2.56	5.258
Thresholding background subtraction	15.56	6.27	8.46	5.23	5.23	2.56

environment, with the imaging system positioned in an adjacent room to emulate realistic through-wall conditions. The "Target type" column specifies the material composition of the targets. For two- and three-target scenarios, the materials are listed in combination (e.g., "metal–wood," "metal–wood–Teflon"). The distances are listed in the same order as the target materials for multi-target scenarios. The "Target description" column provides the size of each target. The progression from single targets (Target IDs 01–15) to two targets (Target IDs 16–27) and then three targets (Target IDs 28–31) demonstrates a systematic increase in complexity. This variation is important in order to test the system's spatial resolution. The systematic variation of key parameters allows for a detailed analysis of the system's strengths and limitations.

In order to evaluate the quality of images, we apply the target-to-clutter ratio (TCR), which is commonly used in SAR image assessment. TWI faces strong reflections from the wall, often overwhelming weaker target signals. High TCR is essential for clear target localization, discrimination of human vs object, and accurate classification or recognition. The TCR indicates the relative strength of clutter (unwanted reflections or interference) compared to the desired signal in a radar or imaging system. It is measured using a statistical method and defining a covariance matrix for clutter and target.

$$\mathrm{TCR} = \frac{\frac{1}{N_t}\sum_{q\in A_t}|I(q)|^2}{\frac{1}{N_c}\sum_{q\in A_c}|I(q)|^2} \tag{7}$$

where A_t and A_c are the target area and clutter area of the image $I(q)$, respectively, and N_t and Nc are the number of image pixels in the target and clutter regions, respectively [16]. Any pixel that does not belong to the target portion region is considered a clutter region.

Single metal and wood targets – image analysis

Metal targets

Metal targets corresponding to Target IDs 01, 04, 07, 10, 13, and 14 were placed behind a wall at varying distances, as detailed in Table 3. The corresponding B-scan images for each target configuration are presented in Figure 2. Various clutter reduction techniques were employed to suppress background clutter and enhance the visibility of the targets. Figure 9 illustrates different targets placed behind the wall at the same and at different distance. These included SVD, SVD-based noise exploitation, the conventional optimal shrinkage algorithm, and thresholding background subtraction. A comparative analysis of these techniques was carried out using the TCR as a performance metric. This analysis provided a quantitative assessment of clutter suppression efficiency and demonstrated the relative effectiveness of each method in enhancing target detection behind the wall. Figure 10 shows the reconstructed images of single metallic targets placed at increasing distances from the wall, ranging from 20 to 200 cm, corresponding to Target IDs 01, 04, 07, 10, 13, and 14, as listed in Table 3. These experiments evaluate the system's ability to detect high-dielectric-contrast targets (metal) and analyze how detection accuracy varies with range.

Table 4 shows and compares the performance of the clutter reduction algorithm based on TCR for a single metallic target. We have observed that at a short distance of 20 cm (Target ID 01), SVD achieves the highest TCR of 17.19 dB, producing a precise and well-focused reconstruction of the metallic target. Thresholding also performs comparably well with a TCR of 15.56 dB, validating its ability to suppress clutter close to the wall. As the target distance increases (e.g., Target IDs 04 and 07), the performance of SVD gradually deteriorates, with TCR dropping to 11.98 and 9.24 dB, respectively. Notably, SVD noise exploitation outperforms conventional SVD for Target ID 04 (TCR = 14.13 dB) by utilizing higher-order singular values to suppress dominant wall echoes while preserving the target's weaker returns. For mid-to-far range targets (IDs 10, 13, and 14), the effectiveness of all techniques diminishes due to increased attenuation and wall clutter.

SVD produces TCRs as low as 3.26 dB for Target ID 14 (200 cm), indicating weak detectability. However, OptShrink remains relatively stable across distances, providing moderate TCR values (e.g., 7.57 dB at ID 07 and 5.26 dB at ID 14), suggesting robustness to range-induced signal degradation. While thresholding offers comparable or better results than SVD for specific mid-range targets, it highlights its potential in scenarios requiring faster computation. The analysis confirms that SVD is most effective for near-range, high-reflectivity targets, while SVD noise exploitation and OptShrink offer better adaptability for complex and longer-range imaging. Thresholding, although simple, proves competitive in short to moderate ranges.

Single wood targets

Figure 11 presents the reconstructed imaging results for single wooden targets placed at varying distances of 20, 50, and 100 cm, corresponding to Target IDs 02, 05, and 12, respectively. In Table 5, the performance of the clutter reduction algorithm is compared based on TCR. Wood has a moderate dielectric constant and reflects less energy than metal, making it more challenging to detect, particularly at greater distances. The reconstructed images were generated using four different clutter suppression techniques: SVD, SVD noise subspace exploitation, OptShrink, and thresholding background subtraction. Their performance is quantified using the TCR metric. For the near-range wood target at 20 cm (Target

https://doi.org/10.1017/S1759078726103468 Published online by Cambridge University Press

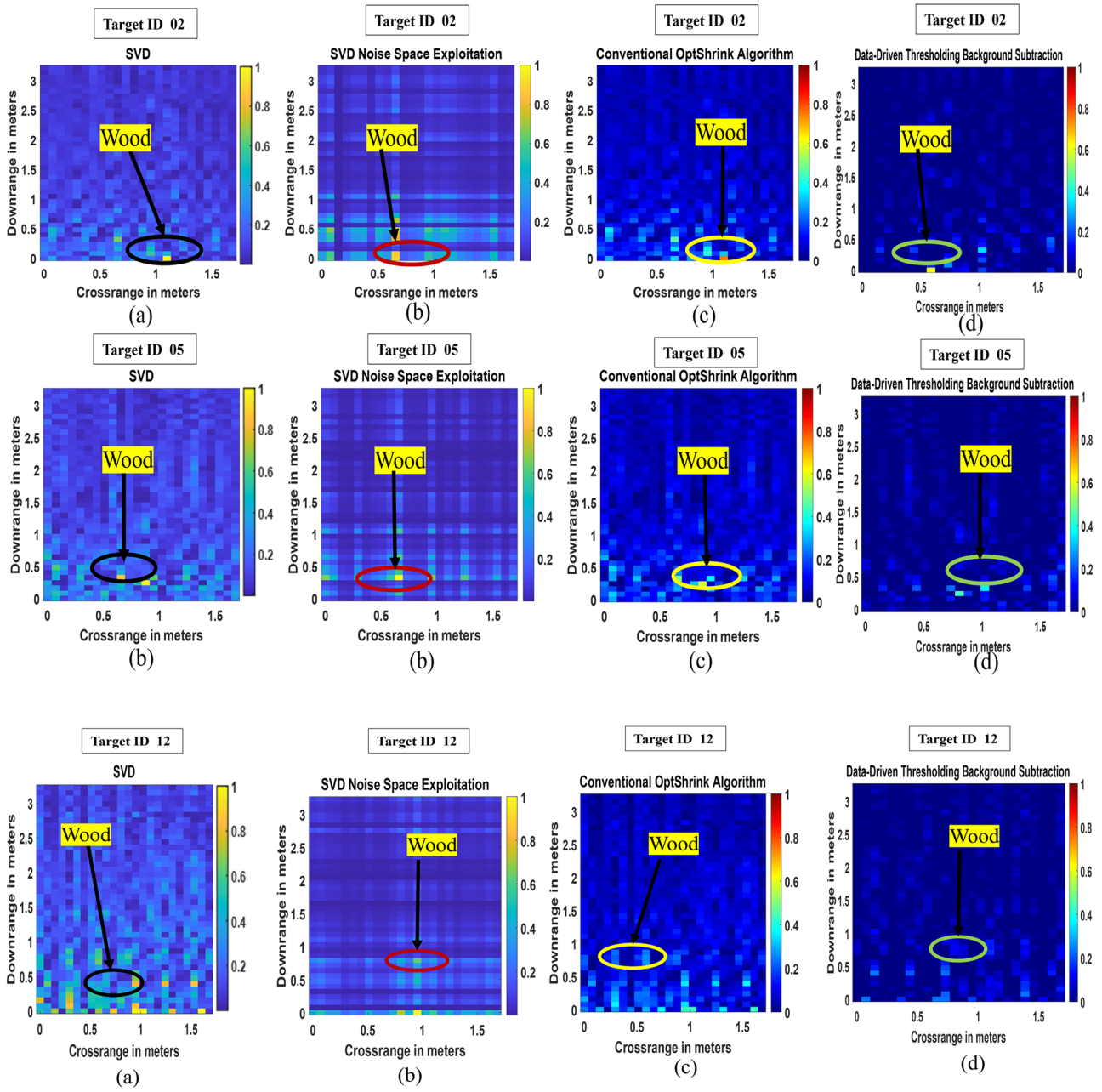


Figure 11. Reconstructed images for woods targets with (a) SVD, (b) SVD noise exploitation, (c) conventional OptShrink algorithm, and (d) thresholding background subtraction.

ID 02), the OptShrink algorithm demonstrated the best clutter suppression performance, achieving a TCR of 6.92 dB, significantly higher than the baseline SVD (4.42 dB). The OptShrink method's low-rank approximation and noise-filtering properties allowed it to enhance subtle target reflections while attenuating wall-related clutter. At a range of 50 cm (Target ID 05), thresholding background subtraction emerged as the most effective technique, delivering a TCR of 7.55 dB.

Its adaptive, data-driven thresholding mechanism likely provided better contrast between the wall background and the target echo. This suggests that statistical thresholding methods can outperform more computationally intensive matrix decomposition

Table 5. Performance of clutter reduction algorithms based on TCR for a single wooden target

Techniques	TCR (dB)		
	Target ID 02	Target ID 05	Target ID 12
SVD	4.42	3.16	0.62
SVD noise exploitation	3.08	1.85	6.63
Convention OptShrink algorithm	6.92	3.88	0.58
Thresholding background subtraction	2.78	7.55	1.84

https://doi.org/10.1017/S1759078726103468 Published online by Cambridge University Press

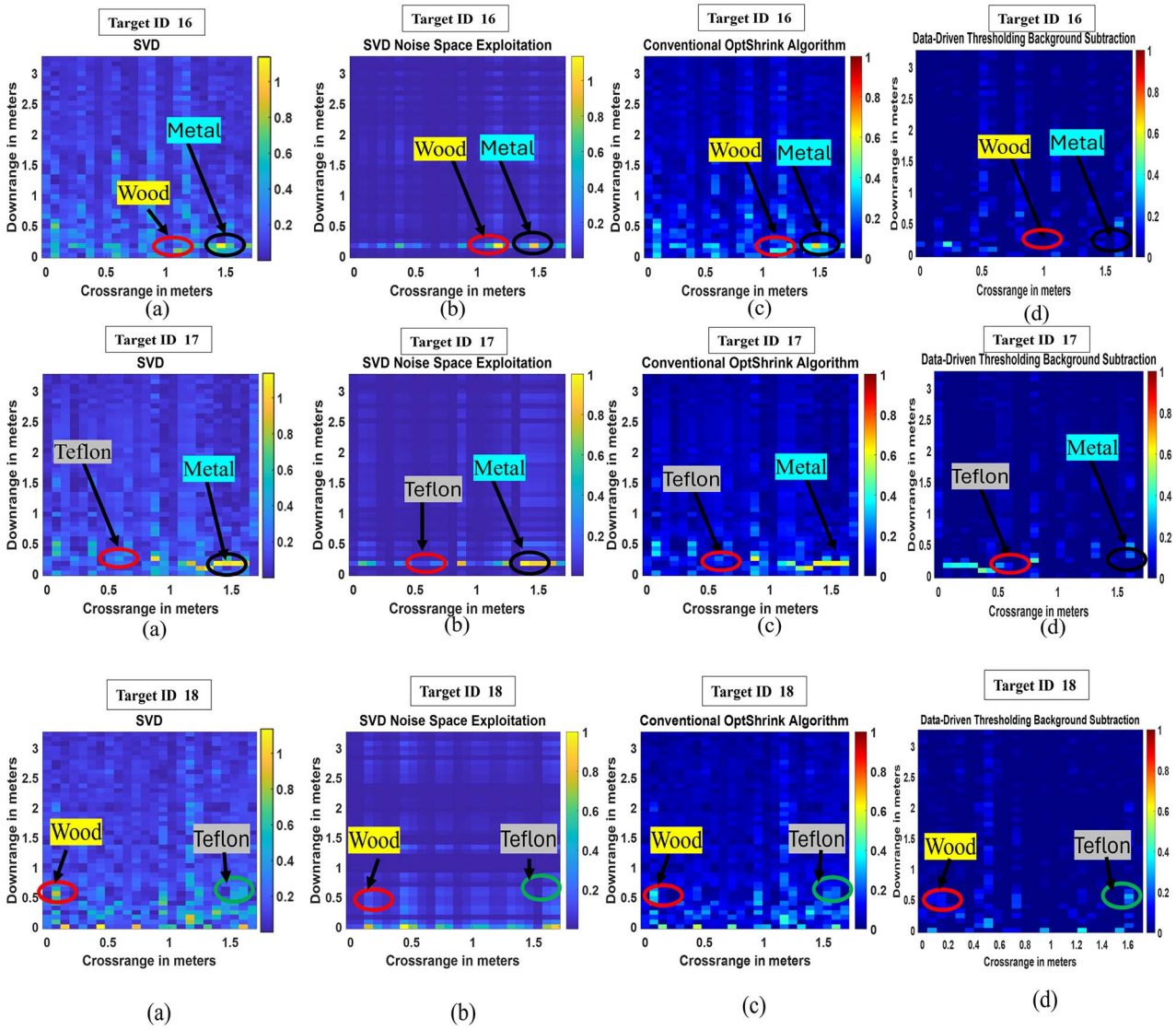


Figure 12. Reconstructed images for multiple targets combination with (a) SVD, (b) SVD noise exploitation, (c) conventional OptShrink algorithm, and (d) thresholding background subtraction.

Table 6. Performance of clutter reduction algorithms based on TCR for two target combinations

Techniques	TCR (dB)		
	Target ID 16	Target ID 17	Target ID 18
SVD	1.78	8.08	4.12
SVD noise exploitation	8.08	11.84	0.26
Convention OptShrink algorithm	5.8	6.72	2.30
Thresholding background subtraction	0.77	0.925	0.63

techniques at moderate distances. In contrast, for the far-range target at 100 cm (Target ID 12), SVD noise exploitation achieved a TCR of 6.63 dB, significantly outperforming all other methods. This method selectively reconstructs signals using higher-order singular components, effectively isolating weak, deeply embedded echoes of low-dielectric targets from dominant wall returns and noise. It demonstrates strong potential for improving detectability in highly cluttered, low-Signal to Noise Ratio (SNR) environments. The conventional SVD method showed only moderate effectiveness in the near field and experienced a sharp performance drop at larger distances, indicating that dominant singular values alone are insufficient for representing weakly reflective targets like wood, especially when signal attenuation increases with distance.

Two targets, a combination of metal, wood, and Teflon

Metal–wood, metal–teflon, and wood–Teflon

For the metal–wood configuration (Target ID 16), the SVD noise exploitation technique exhibited the best performance, achieving a TCR of 8.08 dB, outperforming the OptShrink method (5.80 dB) and standard SVD (1.78 dB). Table 6 compares the performances of clutter reduction algorithm based on TCR for two target combinations. This table suggests that subspace exploitation isolates the weaker wood reflections from the dominant wall

https://doi.org/10.1017/S1759078726103468 Published online by Cambridge University Press

and metal-induced clutter. The thresholding method performed poorly (0.77 dB) in this case, likely due to its inability to handle overlapping strong and weak target responses. In the metal–Teflon case (Target ID 17), which features high reflectivity contrast, SVD noise exploitation again delivered the highest TCR (11.84 dB), highlighting its robustness in resolving both high-strength metallic reflections and low-power Teflon echoes. The basic SVD method also performed well (8.08 dB) due to the distinct separation in signal characteristics between the two materials. OptShrink produced moderate results (6.72 dB), while thresholding failed to adequately suppress clutter, with a TCR of only 0.93 dB.

In contrast, the wood–Teflon combination (Target ID 18) posed the most significant challenge due to the low dielectric contrast of both materials. The standard SVD showed the highest TCR (4.12 dB) among all techniques in this case, likely because it retained sufficient energy from both weak target signals. However, SVD noise exploitation failed (0.26 dB) due to the over-suppression of signals near the noise subspace. Similarly, OptShrink (2.30 dB) and thresholding (0.63 dB) were ineffective, reflecting their limitations in detecting low-SNR overlapping targets. The combined two-target analysis confirms that SVD noise exploitation is highly effective when at least one high-dielectric target (e.g., metal) is present due to its ability to suppress dominant clutter and isolate weaker reflections. Conventional SVD performs well in moderate clutter and high-contrast configurations but lacks adaptability in low-contrast scenarios. OptShrink provides moderate and stable performance across all target types but lacks peak TCR in challenging environments. Figure 12 illustrates the reconstructed images for two target configurations placed at an equal distance of 50 cm behind the wall: metal–wood (Target ID 16), metal–Teflon (Target ID 17), and wood–Teflon (Target ID 18). Each row of subfigures compares the performance of four clutter suppression techniques – SVD, SVD noise subspace exploitation, OptShrink, and thresholding-based background subtraction applied to the same dataset.

Three targets, a combination of metal, wood, and Teflon

The reconstructed images for a combination of three targets using different post-processing techniques are shown in Figure 13. The

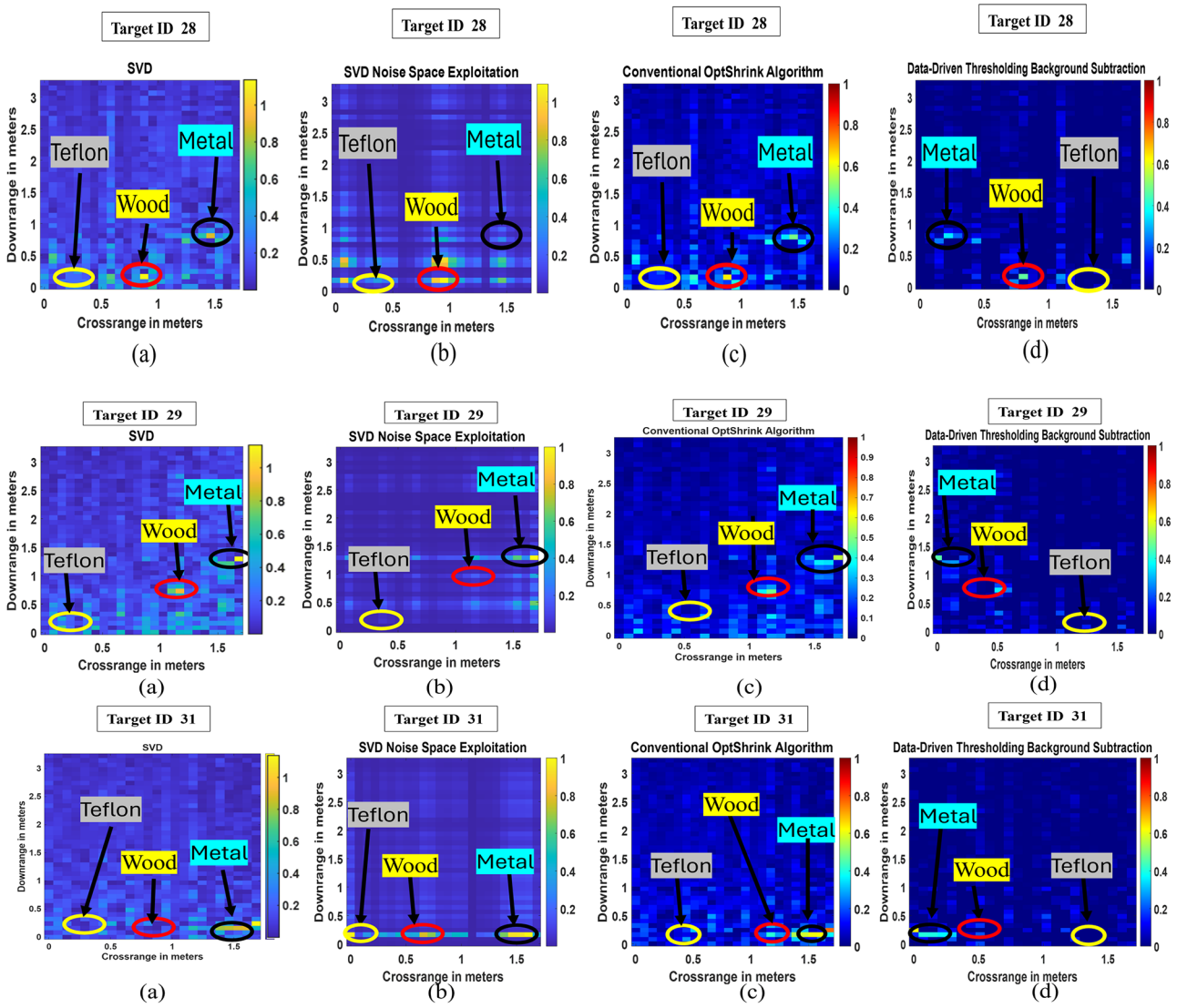


Figure 13. Reconstructed images for multiple targets combination with (a) SVD, (b) SVD noise exploitation, (c) conventional OptShrink algorithm, and (d) thresholding background subtraction.

https://doi.org/10.1017/S1759078726103468 Published online by Cambridge University Press

Table 7. Performance of clutter reduction algorithms based on TCR for three target combinations

Techniques	TCR (dB)		
	Target ID 28	Target ID 29	Target ID 31
SVD	9.93	8.23	10.84
SVD noise exploitation	10.23	6.27	15.58
Convention OptShrink algorithm	7.23	6.20	6.30
Thresholding background subtraction	5.18	4.13	8.75

results show that when all three targets were placed at the same distance (50 cm), both SVD noise exploitation and standard SVD delivered high TCRs (10.23 and 9.93 dB, respectively), indicating their ability to separate overlapping target reflections from wall clutter (see Table 7).

The OptShrink method (7.23 dB) performed moderately well but was limited by its low-rank assumption in complex multipath scenes. Thresholding background subtraction (5.18 dB) showed the lowest effectiveness, consistent with its limitations in scenarios with spatially overlapping clutter. This configuration tested the ability of algorithms to detect targets at significantly different distances. SVD (8.23 dB) marginally outperformed SVD noise exploitation (6.27 dB). The deeper placement of metal and wood targets likely shifted their energy to dominant singular values, which were preserved more effectively by conventional SVD. The OptShrink (6.20 dB) and thresholding (4.13 dB) methods showed reduced performance, reflecting their limited ability to adapt to multi-depth signals with a wide dynamic range. In this asymmetrical distance configuration, SVD noise exploitation achieved the highest TCR of 15.58 dB, clearly outperforming all other methods. This result confirms the strength of noise-space subspace filtering in resolving multi-distance weak targets obscured by wall and multipath clutter. Standard SVD also produced a strong TCR (10.84 dB), followed by thresholding (8.75 dB), which showed surprising effectiveness, likely due to target separation in range. OptShrink, however, remained stable but underwhelming (6.30 dB).

Conclusion

In this work, we have demonstrated the experimental evaluation of a MIMO-based TWI system utilizing various signal and image processing techniques to enhance contrast-based target detection behind walls. The imaging system detected metallic-, wooden-, and Teflon-based targets at varying distances. The choice of clutter removal technique often involves a trade-off between computational efficiency and detection accuracy. SVD noise exploitation is the most effective technique overall, especially in complex and multi-depth scenarios where weak target reflections are obscured by dominant clutter. SVD performs best in high-SNR, shallow target scenarios, especially for strong reflectors like metal. Conventional OptShrink provides consistent but suboptimal results, making it suitable for balanced performance when no extreme clutter or distance variance is present. Thresholding background subtraction, while computationally light, is highly scene-dependent and should not be used as a standalone method for complex or deep-target detection. The results strongly support the development of adaptive or hybrid approaches, wherein clutter suppression techniques are dynamically selected or combined based on scene complexity, target material, and distance.

Competing interests. The authors report no conflict of interest.

References

1. **Ahmad F and Amin MG** (2012) Wall clutter mitigation for MIMO radar configurations in urban sensing. In *2012 11th International Conference on Information Sciences, Signal Processing and Their Applications ISSPA 2012*, pp. 1165–1170. https://doi.org/10.1109/ISSPA.2012.6310467.
2. **Syeda RZ, Savelyev TG, Van Beurden MC and Smolders AB** (2021) Sparse MIMO array for improved 3D mm-wave imaging radar. In *EuRAD 2020 - 2020 17th European Radar Conference*, pp. 342–345. https://doi.org/10.1109/EuRAD48048.2021.00094.
3. **Jamshidi-Zarmehri H, Akbari A, Labadlia M, Kedze K Eucharist, Shaker J, Xiao G and Amaya RE** (2023) A Review on Through-Wall Communications: Wall Characterization, Applications, Technologies, and Prospects. *IEEE Access* **11**, 127837–127854. https://doi.org/10.1109/ACCESS.2023.3331743.
4. **Sengupta A, Jin F, Cuevas RA and Cao S** (2020) A review of recent advancements including machine learning on synthetic aperture radar using millimeter-wave radar. In *IEEE National Radar Conference - Proceedings*, vol. 2020-Septe, Sep. https://doi.org/10.1109/RadarConf2043947.2020.9266501.
5. **Kim GW, Lee SW, Son HY and Choi KW** (2023) A study on 3D human pose estimation using through-wall IR-UWB radar and transformer. *IEEE Access* **11**(February), 15082–15095. https://doi.org/10.1109/ACCESS.2023.3244017.
6. **Tan W, Liu Y and Guo Y** (2021) Study on propagation characteristics of indoor environment at 60 GHz using SBR method. In *2021 International Conference on Microwave and Millimeter Wave Technology (ICMMT 2021) – Proceedings*. https://doi.org/10.1109/ICMMT52847.2021.9617882.
7. **Turk AS, Ozkan-bakbak P, Durak-ata L, Orhan M and Unal M** (2016) High-resolution signal processing techniques for through-the-wall imaging radar systems. *International Journal of Microwave and Wireless Technologies* **8**(6), 855–863. https://doi.org/10.1017/S1759078716000593.
8. **Focsa A, Vladescu A, Toma SA, Gorgoteanu D, Anghel A and Coca M** (2023) Handheld synthetic aperture radar for through the wall imaging: motion errors compensation. *International Geoscience and Remote Sensing Symposium* **2023-July**(Md), 2203–2206. https://doi.org/10.1109/IGARSS52108.2023.10281951.
9. **Bivalkar M, Agarwal S and Singh D** (2022) Development of an efficient approach for detection and measurement of crack length in ceramic tile manufacturing using millimeter-wave imaging. *NDT & E International* **129**, 102656. https://doi.org/10.1016/j.ndteint.2022.102656.
10. **Alvarez-narciandi G, Laviada J and Las-heras F** (2021) Freehand mm-wave imaging with a compact MIMO radar. *IEEE Transactions on Antennas and Propagation* **69**(2), 1224–1229. https://doi.org/10.1109/TAP.2020.3013745.
11. **Zhang C, Kuga Y and Ishimaru A** (2018) Hard-wall radar imaging: Localization of objects shadowed by metallic walls with MIMO Radar. *IEEE Transactions on Antennas and Propagation* **66**(8), 4240–4251. https://doi.org/10.1109/TAP.2018.2835569.
12. **Xu H, Wang B, Zhang J, Liu L, Li Y, Wang Y and Wang A** (2017) Chaos Through-Wall Imaging Radar. *Sens Imaging* **18**(1). https://doi.org/10.1007/s11220-017-0156-9.
13. **Nadakuditi RR** (2014) OptShrink: An algorithm for improved low-rank signal matrix denoising by optimal, data-driven singular value shrinkage. *IEEE Transactions on Information Theory* **60**(5), 3002–3018. https://doi.org/10.1109/TIT.2014.2311661.
14. **Bivalkar MK, Pandey S and Singh D** (2023) An adaptive approach for the detection of contrast targets for the through-wall imaging. *International Journal of Microwave and Wireless Technologies* **15**(3), 424–439. https://doi.org/10.1017/S1759078722000733.
15. **Birnbaum A, Johnstone IM, Nadler B and Paul D** (2013) Minimax bounds for sparse PCA with noisy high-dimensional data. *The Annals of Statistics* **41**(3), 1055–1084. https://doi.org/10.1214/12-AOS1014.

https://doi.org/10.1017/S1759078726103468 Published online by Cambridge University Press

16. **Kawalec A, Ślesicka A and Ślesicki B** (2023) A new statistical method for determining the clutter covariance matrix in spatial–temporal adaptive processing of a radar signal. *Sensors* **23**(9). https://doi.org/10.3390/s23094280.



Suman Anand (SM'25) is currently a Ph.D. research scholar in the Department of Electronics and Communication Engineering at Indian Institute of Technology Roorkee (IIT Roorkee), Roorkee, India. He completed his M.Tech. from the National Institute of Technology Kurukshetra, Haryana, in the year 2021. His research focuses on MIMO-based TWI and signal and image processing. He has published research articles in various conferences.



Dr. **Shailza Gotra** is working as an Assistant Professor in the Department of Electronics and Communication Engineering at LNMIIT, Jaipur, India. She worked as a Research Associate at the Indian Institute of Technology Roorkee. During this period, her research area was the design and development of MIMO-based TWI radar. She completed her PhD in 2021 from the National Institute of Technology Delhi. Her research area includes the advancements in the design and development of dielectric resonator antennas. She was awarded the Mangalagiri's Award for Best Female Student Ph.D. Thesis by the IEEE Women in Engineering (WIE) committee in 2022. She is significantly contributing to the research areas of microwave and millimeter-wave antennas, MIMO antennas, THz graphene antennas, optical nano-antennas, microwave absorbers, and microwave imaging radar systems. She published several high-impact research papers in various reputable journals, including *IEEE Transactions on Antennas and Propagation*. Along with this, she has also reviewed submissions for various reputed journals. She is a member of IEEE, IEEE AP-S, and other professional societies.



Dr. **Vineet Singh** received the Ph.D. degree in Electronics Engineering from the Indian Institute of Technology (BHU), Varanasi, India. He is currently working as an Assistant Professor with the Department of Electronics and Communication Engineering at the National Institute of Technology Patna, India. Prior to joining NIT Patna, he served as a Postdoctoral Research Associate at the Indian Institute of Technology Roorkee, India. His research interests include Doppler signal processing, microwave and millimeter-wave imaging for biomedical diagnostics, non-destructive testing, and solid-state reconfigurable antennas. He has authored several research articles in reputed international journals and conferences and has also contributed to book chapters and patents. Dr. Singh is a member of the Institute of Electrical and Electronics Engineers, IEEE Microwave Theory and Technology Society, IEEE Antennas and Propagation Society, and other professional societies.



Dr. **Mandar Bivalkar** (M'10), born in Maharashtra, India, received an M.Tech. in Electronics and Communication from Dr. Babasaheb Ambedkar Technological University, Lonere, Maharashtra, in 2011 and completed a Ph.D. degree in signal enhancement techniques for microwave imaging at the Indian Institute of Technology Roorkee (IIT Roorkee), Roorkee, India. He possesses more than 23 years of experience in teaching. His research interests include RF and microwave engineering, microwave and MMW imaging, and electromagnetic.



Dr. **Dharmendra Singh** received his Ph.D. in Electronics Engineering from Banaras Hindu University, Varanasi, India. He is currently serving as Director of the Indian Institute of Information Technology Vadodara and as a Professor in the Department of Electronics and Communication Engineering at the Indian Institute of Technology (IIT) Roorkee. He is also a coordinator of the RAILTEL Center of Excellence in Telecom, IIT Roorkee. He has authored and co-authored over 300 papers in various national/international journals and conferences. His main research interests include: Microwave remote sensing, electromagnetic wave interaction with various media, polarimetric and interferometric applications of microwave data, numerical modeling, ground-penetrating radar, and TWI. In the current study, he has framed the flow of study and supervised all the activities of the current research work.

https://doi.org/10.1017/S1759078726103468 Published online by Cambridge University Press